Journal of
Biomedical Optics

BiomedicalOptics.SPIEDigitalLibrary.org

Integrated quantitative phase and birefringence microscopy for imaging malaria-infected red blood cells

Chengshuai Li
Shichao Chen
Michael Klemba
Yizheng Zhu

SPIE.

Chengshuai Li, Shichao Chen, Michael Klemba, Yizheng Zhu, "Integrated quantitative phase and birefringence microscopy for imaging malaria-infected red blood cells," *J. Biomed. Opt.* **21**(9), 090501 (2016), doi: 10.1117/1.JBO.21.9.090501.

Integrated quantitative phase and birefringence microscopy for imaging malaria-infected red blood cells

Chengshuai Li,[a] Shichao Chen,[a] Michael Klemba,[b] and Yizheng Zhu[a,*]
[a]Virginia Tech, The Bradley Department of Electrical and Computer Engineering, 1185 Perry Street, Blacksburg, Virginia 24061, United States
[b]Virginia Tech, Department of Biochemistry, 340 West Campus Drive, Blacksburg, Virginia 24061, United States

Abstract. A dual-modality birefringence/phase imaging system is presented. The system features a crystal retarder that provides polarization mixing and generates two interferometric carrier waves in a single signal spectrum. The retardation and orientation of sample birefringence can then be measured simultaneously based on spectral multiplexing interferometry. Further, with the addition of a Nomarski prism, the same setup can be used for quantitative differential interference contrast (DIC) imaging. Sample phase can then be obtained with two-dimensional integration. In addition, birefringence-induced phase error can be corrected using the birefringence data. This dual-modality approach is analyzed theoretically with Jones calculus and validated experimentally with malaria-infected red blood cells. The system generates not only corrected DIC and phase images, but a birefringence map that highlights the distribution of hemozoin crystals.
[DOI: 10.1117/1.JBO.21.9.090501]

Keywords: spectral multiplexing interferometry; quantitative phase imaging; differential interference contrast; quantitative polarized imaging; hemozoin.

Paper 160257LR received Apr. 21, 2016; accepted for publication Aug. 15, 2016; published online Sep. 6, 2016.

Label-free imaging of biological specimens typically employs optical phase as the primary contrast mechanism, as seen in techniques such as phase contrast microscopy[1] and differential interference contrast (DIC) microscopy,[2] and quantitative phase imaging (QPI) has received growing attention in recent years.[3] In many samples, however, birefringence can offer crucial contrast when revealing fine biological substructures such as collagen,[4] cell membrane,[5,6] mitotic spindle,[7] and hemozoin crystal.[8] Different from phase imaging, in birefringence measurements, one needs to determine two parameters, its retardation as well as the orientation of its axes. Previous attempts on experimental determination of both birefringence parameters often require multiple acquisitions by adjusting polarizing optics, such as waveplates and liquid crystal phase modulators, either mechanically[9–12] or electrically.[13,14]

Functionally, the combination of quantitative phase and birefringence imaging will enhance contrast and may provide additional sample information by comparing registered images of different nature. Such integration, however, is traditionally difficult since the two approaches employ fundamentally different principles and optical setups. A recent advance in quadriwave lateral shearing interferometry has demonstrated such a combination, where birefringence is computed by curve-fitting a series of phase images obtained with a rotating polarizer.[15]

Here, we propose a high-sensitivity spectral interferometry approach. Previously, we have demonstrated a single-shot, quantitative birefringence imaging technique[16] and a quantitative DIC technique for nonbirefringent samples.[17] Implemented with spectral-domain low coherence interferometry for high sensitivity, they were based on similar hardware but unrelated signal analysis and processing. In this letter, we provide a unifying theory to integrate these modalities into a single system for quantitative birefringence, DIC, and phase imaging. Additionally, such theory allows for addressing the issues of system birefringence background and birefringence-induced DIC/phase distortion, thus achieving improved accuracy.

The system setup is based on a common path, reflective interferometer, as shown in Fig. 1(a). It utilizes a broadband superluminescent diode (Superlum; 837 nm, FWHM 54 nm) as the light source. A linear polarizer and a birefringent crystal ($LiNbO_3$, thickness 2.75 mm) are oriented at a predetermined angle to introduce polarization mixing. For quantitative DIC imaging, a Nomarski prism is inserted at the back of the microscope objective (Nikon; 40×, 0.75 NA), splitting o- and e- waves by a small angle that leads to a lateral shear on the sample. Return light will be modified by the crystal and filtered by the polarizer again before being collected by the single-mode fiber. The spectral interference carrying intensity and phase information is then detected by a custom spectrometer. Two galvanometers, separated by a 4-f system, provide two-dimensional (2-D) point scanning of the specimen. For quantitative birefringence imaging, the Nomarski prism is simply removed to eliminate the shear.

Signal propagation through the system can be analyzed with Jones calculus using Fig. 1(b). For convenience, the transmission direction of the polarizer is chosen to be the x-axis. The slow axes of the birefringent crystal and the sample orient at angles α and β relative to the x-axis, respectively. For nonbirefringent samples, β can be any angle since they are optically isotropic and, in fact, it will be eliminated from the equation. System birefringence, arising from the residual birefringence of various system optics, can be treated as a lumped element with its slow axis oriented at angle φ.[14]

We first analyze birefringence imaging, i.e., without the Nomarski prism in Fig. 1(b). Assuming the normalized Jones vector after the polarizer is $[1 \quad 0]^T$, the field after a double-pass transmission through the entire system can be obtained by

$$\begin{aligned}\mathbf{E}_O = [1 \quad 0]\mathbf{R}(-\alpha)\mathbf{T}(\theta_C)\mathbf{R}(\alpha-\varphi)\mathbf{T}(\theta_B)\mathbf{R}(\varphi-\beta)\\ \mathbf{T}(2\theta_S)\mathbf{R}(\beta-\varphi)\mathbf{T}(\theta_B)\mathbf{R}(\varphi-\alpha)\mathbf{T}(\theta_C)\mathbf{R}(\alpha)\begin{bmatrix}1\\0\end{bmatrix},\end{aligned} \tag{1}$$

---

*Address all correspondence to: Yizheng Zhu, E-mail: yizhu1@vt.edu

1083-3668/2016/$25.00 © 2016 SPIE

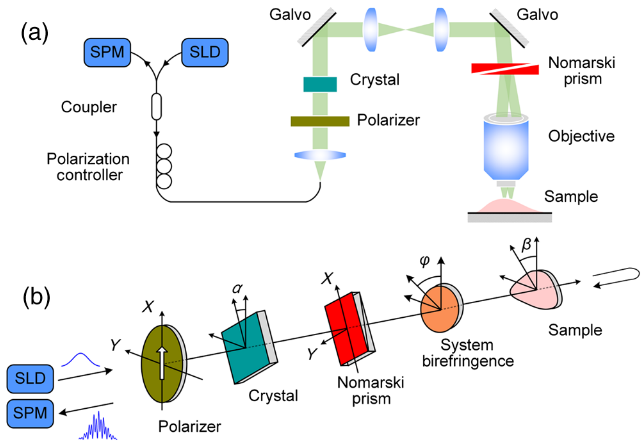

Fig. 1 (a) Schematic of the integrated quantitative phase and birefringence imaging system: SLD, superluminescent diode and SPM, spectrometer. (b) Orientation of polarization components of the imaging system.

where **R** is the rotation matrix and **T** is the transmission matrix for polarizing components, as in

$$\mathbf{R}(\varphi) = \begin{bmatrix} \cos\varphi & \sin\varphi \\ -\sin\varphi & \cos\varphi \end{bmatrix} \quad \text{and} \quad \mathbf{T}(\theta) = \begin{bmatrix} 1 & 0 \\ 0 & e^{j\theta} \end{bmatrix}. \tag{2}$$

Additionally, $\theta_C(k) = kL_C$, $\theta_B(k) = kL_B(x, y)$, and $\theta_S(k) = kL_S(x, y)$, where k is the wavenumber, L_C is the optical path length (OPL) retardation of the crystal retarder, and $L_B(x, y)$ and $L_S(x, y)$ stand for the retardation of system birefringence and sample birefringence at (x, y), respectively.

Since both L_B and L_S in live cell imaging are typically small compared to wavelength, small angle approximation is valid for θ_B and θ_S.[12] With Eqs. (1) and (2), the detected interference spectrum can be shown as

$$\begin{aligned} I &= I_0(k)|\mathbf{E}_O|^2 \\ &= I_{DC}(k) + [I_{1f}(k) + \text{c.c.}] + [I_{2f}(k) + \text{c.c.}], \end{aligned} \tag{3}$$

where $I_0(k)$ is the spectrum envelope

$$\begin{aligned} I_{\mathrm{DC}}(k) &= I_0(k)[\cos^4\alpha + \sin^4\alpha] \\ I_{1f}(k) &= \frac{1}{4}\sin 4\alpha I_0(k)[jA_S(k) + jA_B(k)]e^{jkL_C} \\ I_{2f}(k) &= \frac{1}{4}\sin^2 2\alpha I_0(k)[jB_S(k) + jB_B(k) + 1]e^{j2kL_C}, \end{aligned} \tag{4}$$

and *c.c.* denotes the complex conjugate of corresponding terms. Equation (4) clearly indicates that I_{1f} and I_{2f} are two interference terms in the detected spectrum with carriers of e^{jkL_C} and e^{j2kL_C}, generated by the large OPL retardation of the crystal retarder. In addition, sample and system birefringence parameters are simultaneously modulated onto the complex amplitude of the carrier waves, but are found to be decoupled from each other, as seen in the following intermediate parameters:

$$\begin{aligned} &\begin{cases} A_S(k) = 2\theta_S(k)\sin 2(\alpha - \beta) \\ B_S(k) = 2\theta_S(k)\cos 2(\alpha - \beta) \end{cases}, \\ &\begin{cases} A_B(k) = 2\theta_B(k)\sin 2(\alpha - \varphi) \\ B_B(k) = 2\theta_B(k)\cos 2(\alpha - \varphi) \end{cases}. \end{aligned} \tag{5}$$

Based on the above derivation, we can perform a system birefringence calibration without sample to acquire A_B and B_B and remove them from sample measurement to obtain A_S and B_S only for the determination of sample birefringence parameters.

As for the choice of α, a wide range of angles may be used except when $\sin 4\alpha = 0$ or $\sin^2 2\alpha = 0$ in Eq. (4). A detailed sensitivity analysis and experimental validation for spectral multiplexing interferometry-based birefringence measurement can be found in Ref. 16. Under the small angle approximation here, $I_{\mathrm{DC}}(k)$ is sample independent and the choice of α is flexible. We set α at 31.7 deg so that $\sin 4\alpha = \sin^2 2\alpha$, which leads to identical coefficients for both interference terms in Eq. (4). Thus, the sensitivity of both sample birefringence retardation and azimuth angle will be independent of sample birefringence orientation.[16]

With the knowledge of α, $I_0(k)$ can also be determined from I_{DC}. The signal demodulation hence involves bandpass filtering of I_{1f} and I_{2f}, normalizing them using α and I_0, and frequency downshifting. With the carrier waves obtained from the interference spectra without sample, I_{1f} and I_{2f} can be downshifted to baseband for extracting A_S and B_S from the imaginary part of the complex amplitude after removing A_B and B_B. Sample birefringence is therefore

$$\begin{aligned} L_S &= \mathrm{avg}\left[\sqrt{A_S(k)^2 + B_S(k)^2}/2k\right] \\ \beta &= \mathrm{avg}\left[-\frac{1}{2}\arctan\frac{A_S(k)}{B_S(k)} + \alpha\right], \end{aligned} \tag{6}$$

where $\mathrm{avg}(\cdot)$ denotes averaging over the range of k. This process allows the background-free measurement of L_S and β from one single spectrum.

To demonstrate the birefringence imaging capability, we chose *Plasmodium falciparum*-infected human red blood cells (RBCs). During their asexual replication cycle within RBCs, malaria parasites consume host cell hemoglobin and produce birefringent hemozoin crystals. For imaging, an *in-vitro* culture of *P. falciparum*-infected erythrocytes was fixed with 0.1% glutaraldehyde in phosphate-buffered saline (PBS). Fixed parasites were then washed with PBS to remove glutaraldehyde prior to imaging.

To quantify RBC birefringence, we first calibrate system birefringence background with a gold mirror. Its magnitude map is shown in Fig. 2(a), with an averaged retardation of 4.12 nm over the field of view. The spatial and temporal sensitivity for birefringence measurement have also been experimentally determined. Since A_S and B_S are both Gaussian random variables, Eq. (6) implies the birefringence retardation L_S is a Raleigh distribution. This is confirmed by the calibration results in Figs. 2(c) and 2(d), with $\sigma_s = 31.7$ pm for full field spatial sensitivity and $\sigma_t = 23.3$ pm for single spot temporal sensitivity.

Figure 2(e) shows the birefringence retardation image of the RBCs after background subtraction based on Eqs. (4) and (5). Among the imaged cells, the infected ones can be clearly identified by the hemozoin crystals inside. The magnitude of hemozoin birefringence retardation in the infected RBCs is about 30 nm and is much stronger than the birefringence of the cell

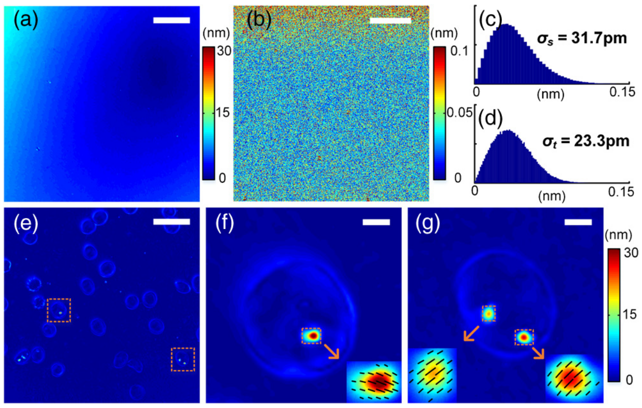

Fig. 2 (a) System birefringence background. Scale bar 20 μm. (b) Spatial sensitivity of birefringence retardation. Scale bar 20 μm. (c) Birefringence retardation histogram of full field in (b). (d) Temporal sensitivity of birefringence retardation. (e) Birefringence retardation image of *P. falciparum*-infected human RBCs. Scale bar 20 μm. (f) and (g) Birefringence retardation images of single infected RBCs from (e). Scale bar 2 μm. Inset: the line direction and length indicate the local optical axes orientation and birefringence retardation of the hemozoin crystals.

body, which is believed to be originated largely from local heterogeneity. Enlarged images of two infected RBCs are also depicted in Figs. 2(f) and 2(g) with slow axis orientation illustrated. One and two crystals are revealed with the birefringence slow axis distributed uniformly for each crystal, respectively. The presence of two crystals likely indicates that this red cell has been invaded by two parasites.

In addition to single-shot birefringence imaging, the same setup can also be used for quantitative DIC imaging. Note that as shown in Fig. 1(b), the direction of the inserted Nomarski prism should be parallel to the axes of the crystal retarder. With the Nomarski prism splitting the incident beam into two by a small angle, the o- and e- waves will experience different polarization mixing in the specimen. The Jones analysis now becomes

$$\begin{aligned}\mathbf{E}_O = [1 \quad 0]\mathbf{R}(-\alpha)\mathbf{T}(\theta_C)\mathbf{R}(\alpha-\varphi)\mathbf{T}(\theta_B)\mathbf{R}(\varphi-\alpha)\\ \cdot\left[\mathbf{R}(\alpha-\beta)\mathbf{T}_{S1}\mathbf{R}(\beta-\alpha)\begin{pmatrix}1 & 0\\ 0 & 0\end{pmatrix}\right.\\ \left.+\mathbf{R}(\alpha-\beta)\mathbf{T}_{S2}\mathbf{R}(\beta-\alpha)\begin{pmatrix}0 & 0\\ 0 & 1\end{pmatrix}\right]\\ \cdot\mathbf{R}(\alpha-\varphi)\mathbf{T}(\theta_B)\mathbf{R}(\varphi-\alpha)\mathbf{T}(\theta_C)\mathbf{R}(\alpha)\begin{bmatrix}1\\ 0\end{bmatrix},\end{aligned} \tag{7}$$

where $\mathbf{T}_{S1}$ and $\mathbf{T}_{S2}$ denote the respective transmission matrices for sample retardation for the two waves at their corresponding positions,

$$\mathbf{T}_{S1} = \begin{pmatrix} e^{j2kL_{1e}} & 0\\ 0 & e^{j2kL_{1o}}\end{pmatrix} \quad \text{and} \quad \mathbf{T}_{S2} = \begin{pmatrix} e^{j2kL_{2e}} & 0\\ 0 & e^{j2kL_{2o}}\end{pmatrix}. \tag{8}$$

Similar to birefringence imaging, Eq. (7) is expanded and the second interference term $(2f)$ can be obtained as

$$\begin{aligned}I_{2f} = \frac{1}{4}\sin^2 2\alpha I_0(k)e^{jk(L_{2e}-L_{1e}+L_{2o}-L_{1o})}\\ \times[jB_S(k)+jB_B(k)+1]e^{j2kL_C}.\end{aligned} \tag{9}$$

For nonbirefringent samples, the o- and e- waves are identical. When system birefringence is also ignored, Eq. (9) can be simplified to

$$I_{2f} = \frac{1}{4}\sin^2 2\alpha I_0(k)e^{j2k(L_2-L_1)}e^{j2kL_C}, \tag{10}$$

which, as expected, is essentially identical to the previously reported expression.[18] The quantitative DIC signal is simply the phase of downshifted I_{2f}.

In contrast, for birefringent samples, the OPL gradient term in I_{2f} is $e^{jk(L_{2e}-L_{1e}+L_{2o}-L_{1o})}$. It can be interpreted as the average OPL gradients of o- and e- waves. Also, we have an additional complex term, $[jB_S(k)+jB_B(k)+1]$, which is determined by system and sample birefringence. This birefringence-induced coefficient thus introduces a phase error in OPL gradient measurement. Fortunately, it is identical to the term in I_{2f} in Eq. (4) and is, therefore, already known from birefringence measurement. As a result, the birefringence-induced phase error can be corrected using the birefringence data.

Figures 3(a) and 3(b) show the OPL gradient images before and after the birefringence correction. In Fig. 3(c), closer examination of these DIC data reveals a clear difference at the position of hemozoin crystal. The corrected positive and negative DIC peaks (blue) become symmetric about zero, which is a typical indication of birefringence-free DIC signal. This confirms that the phase error from sample anisotropy has been removed effectively. We also observe that, for low-birefringence areas away from the hemozoin, the OPL gradient data before and after correction are still in good agreement. The OPL gradient images of the infected RBCs after correction are also given in Figs. 3(d) and 3(e) for horizontal and vertical shear directions, respectively.

Further, with these two directional OPL gradient images and 2-D phase reconstruction algorithms,[19,20] quantitative phase image of the sample can be obtained, as shown in Fig. 4(a). The process involves image registration between the two gradient images and FFT-based 2-D phase integration.

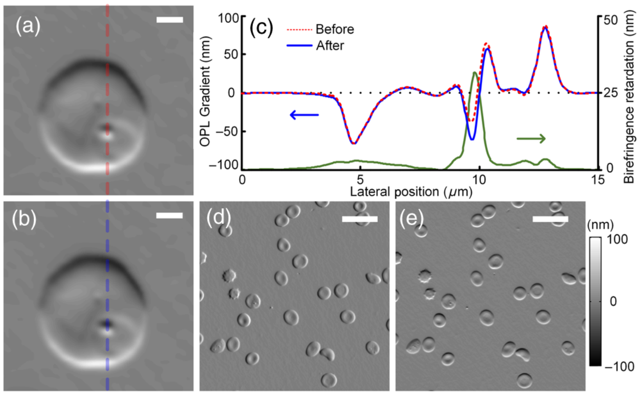

Fig. 3 DIC gradient of an infected RBC (a) before and (b) after phase distortion correction. Scale bar 2 μm. (c) Red and blue curves are the OPL gradient along the lines in (a) and (b). Green curve is the sample birefringence retardation along the same line. (d) and (e) Corrected DIC images of RBCs with horizontal and vertical shear, respectively.

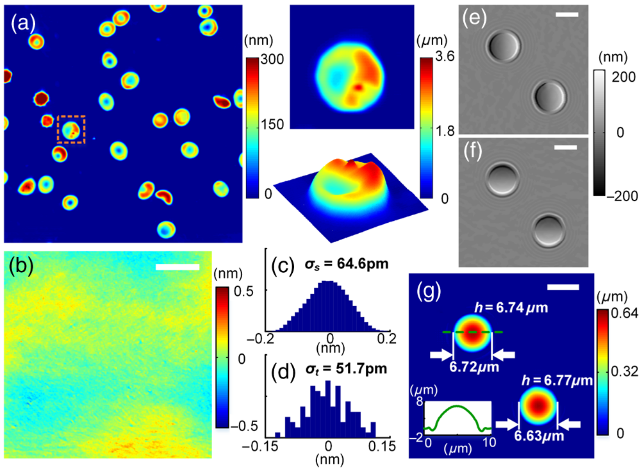

Fig. 4 (a) Quantitative phase image based on 2-D integration of Figs. 3(d) and 3(e). Enlarged 2-D absolute height image and three-dimensional (3-D) representation of the infected cell shown in Fig. 2(c). (b) Spatial sensitivity of QPI. Scale bar 20 μm. (c) Quantitative phase histogram of full field in (b). (d) Temporal sensitivity of QPI. (e) and (f) DIC images of silica microspheres with horizontal and vertical shear, respectively. Scale bar 5 μm. (g) Quantitative phase image based on (e) and (f), labeled with microsphere width and height. Inset: absolute height curve along the dashed line across the upper microsphere.

The spatial and temporal sensitivity of the integrated phase are also calibrated using a gold mirror. The spatial sensitivity is $\sigma_s = 64.6$ pm across the full field, as seen in Figs. 4(b) and 4(c). The temporal sensitivity calculated from 100 consecutive acquisitions is shown in Fig. 4(d) with a noise level of $\sigma_t = 51.7$ pm. The QPI accuracy has also been validated with silica microsphere size standards (Corpuscular Inc., $\Phi = 6.4$ μm, aqueous suspension). The physical width and height of silica microspheres, converted from quantitative phase data and labeled in Fig. 4(g), are consistent with the manufacturer's specification.

In conclusion, we have proposed and demonstrated a dual-modality system for quantitative birefringence and phase imaging. Imaging modes can be easily switched by the insertion and removal of a Nomarski prism. A unified theoretical treatment provides a rigorous foundation for both techniques. From the theory, a process for system birefringence background subtraction is derived to improve birefringence measurement accuracy. This is particularly important for imaging live cells, whose birefringence is often weak and can be significantly distorted by background. The theory also enables the correction of birefringence-induced phase error, thus opens doors to precision phase imaging of birefringent samples. One limitation of the current system is that only in-plane birefringence is measured. Potentially, multiangle measurement would provide more complete information on 3-D anisotropy. Experiments on *P. falciparum*-infected human RBCs demonstrate the system's capability for highly sensitive birefringence, DIC, and phase imaging. Hemozoin crystals are visualized with high contrast and can potentially be used for quantitative study of crystal formation and growth. This highly integrated system may find applications in label-free imaging of biological specimens where multiple intrinsic contrasts are desired.

References

1. F. Zernike, "Phase contrast, a new method for the microscopic observation of transparent objects," *Physica* **9**(7), 686–698 (1942).
2. G. Nomarski, "Differential microinterferometer with polarized waves," *J. Phys. Radium* **16**(9), 9S–11S (1955).
3. G. Popescu, *Quantitative Phase Imaging of Cells and Tissues*, McGraw Hill Professional, New York (2011).
4. A. Changoor et al., "A polarized light microscopy method for accurate and reliable grading of collagen organization in cartilage repair," *Osteoarthritis Cartilage* **19**(1), 126–135 (2011).
5. L. B. Cohen, R. D. Keynes, and B. Hille, "Light scattering and birefringence changes during nerve activity," *Nature* **218**(5140), 438–441 (1968).
6. Y. Abraham and R. Elbaum, "Quantification of microfibril angle in secondary cell walls at subcellular resolution by means of polarized light microscopy," *New Phytol.* **197**(3), 1012–1019 (2013).
7. R. Oldenbourg, E. D. Salmon, and P. T. Tran, "Birefringence of single and bundled microtubules," *Biophys. J.* **74**(1), 645–654 (1998).
8. A. K. Dharmadhikari et al., "On the birefringence of healthy and malaria-infected red blood cells," *J. Biomed. Opt.* **18**(12), 125001 (2013).
9. Y. Otani et al., "Two-dimensional birefringence measurement using the phase shifting technique," *Opt. Eng.* **33**(5), 1604–1609 (1994).
10. Z. Wang et al., "Jones phase microscopy of transparent and anisotropic samples," *Opt. Lett.* **33**(11), 1270–1272 (2008).
11. H. Shin, S.-M. Shin, and D. Y. Kim, "New, simple theory-based, accurate polarization microscope for birefringence imaging of biological cells," *J. Biomed. Opt.* **15**(1), 016028 (2010).
12. J. Park et al., "LCD panel characterization by measuring full Jones matrix of individual pixels using polarization-sensitive digital holographic microscopy," *Opt. Express* **22**(20), 24304–24311 (2014).
13. Y. Zhu, T. Takada, and Y. Murooka, "Two-dimensional optical measurement techniques based on optical birefringence effects," *Opt. Eng.* **41**(12), 3183–3192 (2002).
14. M. Shribak and R. Oldenbourg, "Techniques for fast and sensitive measurements of two-dimensional birefringence distributions," *Appl. Opt.* **42**(16), 3009–3017 (2003).
15. S. Aknoun et al., "Quantitative retardance imaging of biological samples using quadriwave lateral shearing interferometry," *Opt. Express* **23**(12), 16383–16406 (2015).
16. C. Li and Y. Zhu, "Quantitative polarized light microscopy using spectral multiplexing interferometry," *Opt. Lett.* **40**(11), 2622–2625 (2015).
17. C. Li and Y. Zhu, "Spectral-domain interferometry for quantitative DIC microscopy," *Proc. SPIE* **8949**, 89491D (2014).
18. Y. Zhu et al., "Spectral-domain differential interference contrast microscopy," *Opt. Lett.* **36**(4), 430–432 (2011).
19. M. R. Arnison et al., "Linear phase imaging using differential interference contrast microscopy," *J. Microsc.* **214**(1), 7–12 (2004).
20. P. Bon, S. Monneret, and B. Wattellier, "Noniterative boundary-artifact-free wavefront reconstruction from its derivatives," *Appl. Opt.* **51**(23), 5698–5704 (2012).